

Inverse Design of Mechanical Metamaterials that Undergo Buckling

Giorgio Oliveri,¹ Johannes T.B. Overvelde,^{1*}

AMOLF, Science Park 104, 1098 XG Amsterdam, Netherlands

*To whom correspondence should be addressed; E-mail: overvelde@amolf.nl

February 5, 2020

Abstract

Metamaterials are man-made materials which get their properties from their structure rather than their chemical composition. Their mesostructure is specifically designed to create functionalities not found in nature. However, despite the broad variety of metamaterials developed in recent years, a straightforward procedure to design these complex materials with tailored properties has not yet been established. Here we tackle the inverse design problem by introducing a general optimization tool to explore the range of properties that can be achieved. Specifically, we use a stochastic optimization algorithm to solve disjoint problems, focus on optimizing the buckling properties of mechanical metamaterials, including experimental verification of our predictions. Besides this problem, our algorithm can be applied to a large variety of systems that, because of their complexity, would be challenging otherwise. Potential applications range from the design of optomechanical resonators, acoustic band gap materials, to dielectric metasurfaces.

Introduction

Metamaterials are materials that derive their properties from their structure, not only from their chemical composition. The microstructure of these materials is specifically designed to create new functionalities not found in nature, such as materials characterized by a negative index of refraction [1, 2], negative Poisson's ratio [3], and a very high stiffness to weight ratio [4], or structures that enable optical [5] and mechanical [6] cloaking. While most of the properties of these metamaterials are fixed, compliance, resulting from the use of soft or relatively thin materials, can be used as a paradigm to design reconfigurable metamaterials with tunable functionality.

A particularly interesting avenue has been to harness mechanical instabilities in the design of reconfigurable metamaterials, which changes the continuous nature of the transformation to a discrete response originating from bifurcation. Interestingly, these instabilities can be used to increase the sensitivity to external loads, and enable multistability and hysteretic behavior [7]. In contrast to the complex and unstable behavior that these mechanical metamaterials show, their architecture is often surprisingly simple. One of the iconic examples is an elastomeric material patterned with a square lattice of circular pores [8]. Upon compression, a collective buckling instability suddenly changes the Poisson's ratio from positive to negative, and in a similar fashion changes the phononic behavior by opening and closing band gaps [9]. While several studies focused on the effects of pore shape [10], pore distribution [11] and material loading direction [12], the mechanical properties have only been tuned within limits dictated by a few geometrical parameters. Here, design optimization approaches could play a key role in solving the inverse problem to design mechanical metamateri-

als with specific properties, and explore the bounds of achievable functionality.

A specific inverse design approach that has been successfully applied to a large variety of problems is called topology optimization. This method has been developed to allow for complete design freedom by varying the local density of the structure, and therefore does not require a description and parametrization of the geometry beforehand [13]. While topology optimization was initially used to solve mechanical design problems such as maximizing structural stiffness using a limited amount of material [14, 15, 16], it gradually expanded towards other research areas such as optics [17, 18, 19, 20], phononics [21], material science [22, 23, 24], and fluid mechanics [25]. Importantly, most of the algorithms use gradient information of the objective function and constraints to reach a local or global minimum. Therefore, the optimization problem needs to be continuous and differentiable with respect to the design variables. While some work has been done to include buckling behavior in the optimization problem either through constraints [26] or the objective function [27, 16], the requirement of gradient information complicates the applicability and generalization of these approaches. Moreover, the presence of multiple local minima makes the optimization highly dependent on the initial conditions [28] and search algorithm.

Here, . To reduce the search space and to generate smooth structures, we introduce a heuristic subroutine inspired by the ferromagnetic Ising model. More specifically, we show how it is possible to design structures with maximum buckling load, but also allow tailoring to a predefined buckling force within a wide range of values. We furthermore show that by controlling the occurrence of higher modes, we can effectively remove multi-mode interactions that occur

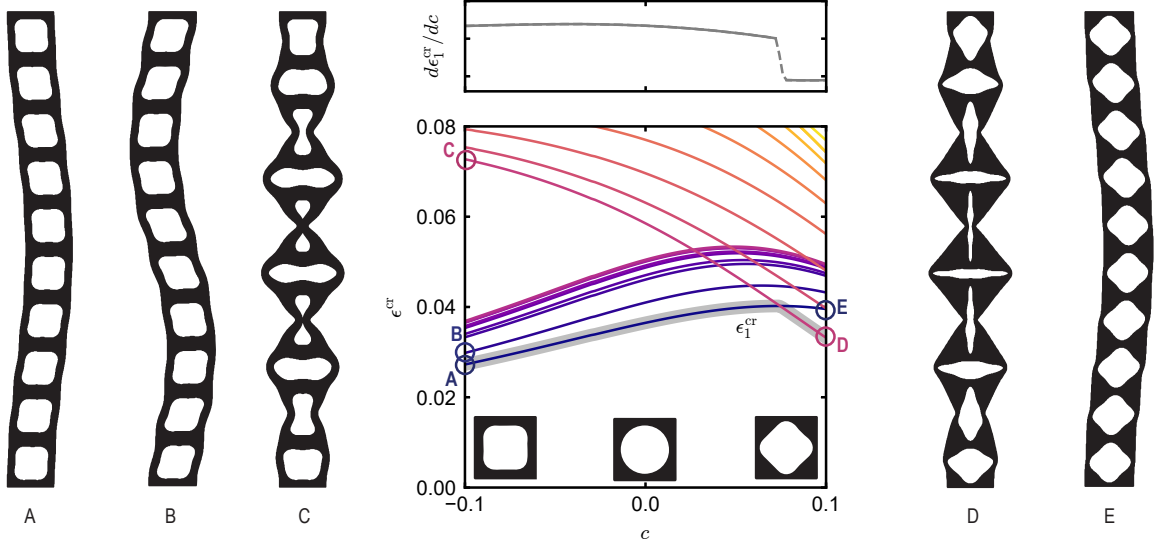


Figure 1: FEA simulation results showing the effect of pore shape on the buckling behavior of periodic porous beams under vertical compression. Here the first twenty modes are shown. Since mode switching occurs at $c = 0.075$, the buckling strain of the first mode ϵ_1^{cr} is not continuously differentiable, such that gradients based optimization algorithms cannot be applied to optimize buckling behavior.

for nearly degenerate bifurcations. Finally, we validate our optimized designs using compression experiments on elastomeric samples. While the performances of gradient based topology optimization algorithms have been proven to be unmatched [28], here we show that stochastic algorithms, due to their flexibility and relative simplicity of implementation, provide a general approach beneficial to explore more complex problems.

Problem description

To emphasize how the morphology of a structure can alter its buckling behavior in a discontinuous fashion, we performed a buckling analysis on a range of beams with different pore shape. Each beam is composed of $n = 10$ vertically placed square unit cells that contain a pore defined by a geometrical parameter c . The

radius of the pore shape is defined as [10]

$$r(\theta) = \frac{L\sqrt{2\phi}}{\sqrt{\pi(2+c^2)}} [1 + c \cos(4\theta)], \quad (1)$$

in which $0 \leq \theta \leq 2\pi$, L is the size of the unit cell and ϕ the porosity. We applied a vertical compressive strain on beams with a porosity $\phi = 0.5$, and ran linear buckling analyses for $-0.1 \leq c \leq 0.1$ using the Finite Element Analysis (FEA) package Abaqus, in which we discretized the structure using biquadratic plane stress elements (CPE8R). In Figure 1 we show the critical strain ϵ^{cr} for the first 20 buckling modes as a function of the pore shape. By monitoring the displacement of 11 nodes along the longitudinal axis of the beams, we were able to correlate the mode shape between the different beams via bivariate correlation [29]. This enables us to identify mode switching that arises from changes in pore geometry.

We next focus on the buckling mode with the lowest critical strain, since this mode will occur upon compression of the beam. We find that for $c < 0.075$ the buckling mode of the beam is characterized by a typical macroscopic buckling mode with a wavelength of $2nL$ that is equal to twice the length of the beam, while for $c > 0.075$ a microscopic buckling mode occurs characterized by a wavelength of $2L$ equal to twice the size of the unit cell [30, 31]. When we would perform an optimization to e.g. maximize the lowest critical strain of the beam according to

$$\max_c \epsilon_1^{\text{cr}}, \quad (2)$$

we find that the derivative of the objective function $d\epsilon_1^{\text{cr}}/dc$ is discontinuous due to the change in buckling behavior (Fig. 1). This strengthens the need of optimization techniques that do not rely on gradient information to seek the

optimum.

Stochastic optimization

In order to find structures with interesting and specific buckling behavior, we developed a density-based stochastic topology optimization approach based on the geometrical description used in the SIMP interpolation method [32, 33]. The topology of the structure, which is divided into square elements, can be changed by varying the density of the elements between $0 \leq \rho_i \leq 1$. Differently, in our stochastic optimization implementation we can use a discrete representation of the design since we do not require intermediate unrealistic densities to make our design continuously differentiable [34]. As such, we assume that each element can take a density ρ_i of $\rho_{\min} \approx 0$ (void) or $\rho_{\max} = 1$ (solid). When assuming linear elastic behavior of each element, we can evaluate the initial mechanical and buckling response of the structures by using a linear FEA code implemented in Matlab (details in Sec. 1 of the SI), in which the stiffness and Poisson's ratio of each element are given by $E_i = \rho_i E$ and $\nu_i = \rho_i \nu$ to account for the geometry of the structure.

Starting from an initial random density distribution with a solid/void ratio of ϕ , we alter the geometry by randomly picking and exchanging two elements with different density. After each change in geometry, the objective function $\Phi(\rho_i)$ is evaluated. Following a simulated annealing optimization approach [35], the variation in objective function $\Delta\Phi(\rho_i)$ between current and previous iteration is used to determine the acceptance probability, $P(\Delta\Phi(\rho_i))$ of the new candidate solution according to

$$P(\Delta\Phi(\rho_i)) = e^{-\frac{\Delta\Phi(\rho_i)}{T}}, \quad (3)$$

where T is a parameter often referred to as the *Temperature*, which can be used to tune the acceptance probability of optimization steps that do not improve the objective function, in order to reach global optima. Here we use a fixed number of iterations for the optimization, N_{iter} , and assume an exponential decay of the temperature [35, 36]. We let the temperature decrease from T_{max} to T_{min} , such that the temperature at a given iteration n is given by

$$T(n) = T_{\text{max}} \left(\frac{T_{\text{min}}}{T_{\text{max}}} \right)^{n/N_{\text{iter}}}. \quad (4)$$

A test problem: compliance optimization

While our main goal is to optimize buckling behavior, we will first test our method using a typical topology optimization problem that is computationally less expensive. We focus on compliance optimization (i.e. stiffness maximization), and do this by replicating the MBB-beam optimization problem [37, 38] (see schematic in Fig. 2a). This allows us to compare our implementation with previous work. If we consider a domain with $n_x \times n_y = 60 \times 20$ elements, the optimization problem can be formulated as:

$$\min_{\rho_i} \quad \Phi(\rho_i) = C = \{\mathbf{D}\}^T [\mathbf{K}] \{\mathbf{D}\}, \quad (5a)$$

$$s.t. \quad \{\mathbf{F}\} = [\mathbf{K}] \{\mathbf{D}\}, \quad (5b)$$

$$\frac{V_{\text{solid}}}{V_{\Omega}} = \phi^* = 0.5, \quad (5c)$$

where $\{\mathbf{D}\}$ and $\{\mathbf{F}\}$ are vectors containing the displacement and reaction forces at the nodes, respectively, which are related by the stiffness matrix $[\mathbf{K}]$ (see Sec. 1 of the SI). Moreover, the volume constraint of Eq. 5c enforces that the ratio between the volume of material elements, V_{solid} , and the total domain

volume, V_Ω , is constant. Note that in our approach this volume constraint is automatically satisfied, and depends on the initial solid/void fraction. Finally, we normalize the compliance of our designs C by the compliance of a homogeneous structure C_{ref} with $\rho_i = 0.5$, such that $\tilde{C} = C/C_{\text{ref}}$.

We start by identifying proper temperature bounds (T_{max} and T_{min}) for the simulated annealing algorithm (Eq. 4). First, to determine the objective function sensitivity to the temperature, we run 10 optimizations with a total number of iterations equal to $N_{\text{iter}} = 1.5 \times 10^4$, during which the temperature is decreased according to Eq. 4 between $T_{\text{max}} = 10^2$ and $T_{\text{min}} = 1 \times 10^{-9}$. By looking at the objective function evolution for decreasing T (Fig. 2a), we identify three regimes. (i) For high temperatures ($T > 20$) any candidate solution is accepted, such that the objective function fluctuates around the same value and there is no convergence to an optimum. (ii) Intermediate temperatures ($1 \times 10^{-7} \leq T \leq 20$) result in convergence towards a minimum, with a probability to reach a global minimum. (iii) For $T < 1 \times 10^{-7}$ only candidate solutions with lower objective function are accepted, the algorithm behaves as a random search with steepest descent and therefore only converges to a local minimum. For optimal behavior of the simulated annealing algorithm, we focus on regime (ii), such that $T_{\text{max}} = 20$ and $T_{\text{min}} = 1 \times 10^{-7}$.

Using these specific bounds for the temperature, we next focus on finding the required number of iterations N_{iter} . To do so, we performed several optimizations with $500 \leq N_{\text{iter}} \leq 15000$. In Figure 2b we show the final objective function values for 30 optimizations per data point. As expected, we find that a larger number of iterations (i.e. a slower cooling rate) benefits the objective function optimization. This can also be seen by looking at the topologies asso-

ciated with different cooling rates (Fig. 2b), which become more clustered given enough time. Balancing the time required for the optimization with the final objective function value, $N_{\text{iter}} = 10^4$ seems to be a good choice for the number of iterations, for which the typical $\tilde{C} \approx 0.9$.

Ising-inspired subroutine

As can be seen from the compliance optimization examples (Fig. 2b), while the solutions are converging, the current approach leads to structures with fragmentation and local checkerboard patterns. This is a typical problem in topology optimization, and is the result of artificial stiffening [39, 40]. As a result, the optimized geometries highly depends on the choice of mesh density. Moreover, apart from introducing numerical artifacts, these local patterns make the fabrication impossible.

Typically, this problem is solved by introducing local averaging [41], which is not suitable for our optimization given that we do not take into account intermediate densities. , we introduce an approach to heuristically reduce the probability of certain geometrical features by drawing only specific candidate solutions. Here, we take inspiration from the 2D ferromagnetic Ising Model [42, 43], and implement a subroutine to prioritize clustering of the material, . While the Ising model describes the behavior of a system formed by magnetic dipole moments of different spins interacting among each other, we translate the spin diversity into material diversity. If we relate the spin to the density of each element according to $s_i = 2\rho_i - 1$, using the Von Neumann neighborhood

the total energy in our system can be written as

$$E = -\frac{1}{2} \sum_{i=1}^{N_{\text{elem}}} s_i [s_{\text{up}(i)} + s_{\text{down}(i)} + s_{\text{left}(i)} + s_{\text{right}(i)}], \quad (6)$$

where the spin of each element s_i is only affected by the spins of the four adjacent elements. Therefore, if an element of a certain spin s_i is inverted, the system will experience a variation in Ising Energy equal to

$$\Delta E_i = 2 s_i [s_{\text{up}(i)} + s_{\text{down}(i)} + s_{\text{left}(i)} + s_{\text{right}(i)}], \quad (7)$$

which, according to the 2D Ising Method, is only accepted with a probability equal to

$$P(\Delta E_i) = e^{-\frac{\Delta E_i}{T_{\text{Ising}}}}. \quad (8)$$

Here, the Ising temperature T_{Ising} can be used to tune the acceptance probability of certain topological variations. Lower T_{Ising} will result in the formation of more clustered candidates solutions, while higher T_{Ising} will not have much effect on the selection of the candidate solution and therefore will result in topologies similar to those shown in Fig. 2b.

Note that for the Ising model, especially for low temperatures, it often occurs that no spins changes are made during a step. To make sure that our design changes in each iteration step, we instead draw an element from the probability distribution specified by

$$P(S_i) = \frac{P(\Delta E_i)}{\sum_{k=1}^{N_{\text{elem}}} P(\Delta E_k)}, \quad (9)$$

which depends on how the Ising acceptance probability of an element $P(\Delta E_i)$ relates to the total acceptance probability $\sum_{k=1}^{N_{\text{elem}}} P(\Delta E_k)$ of the current state.

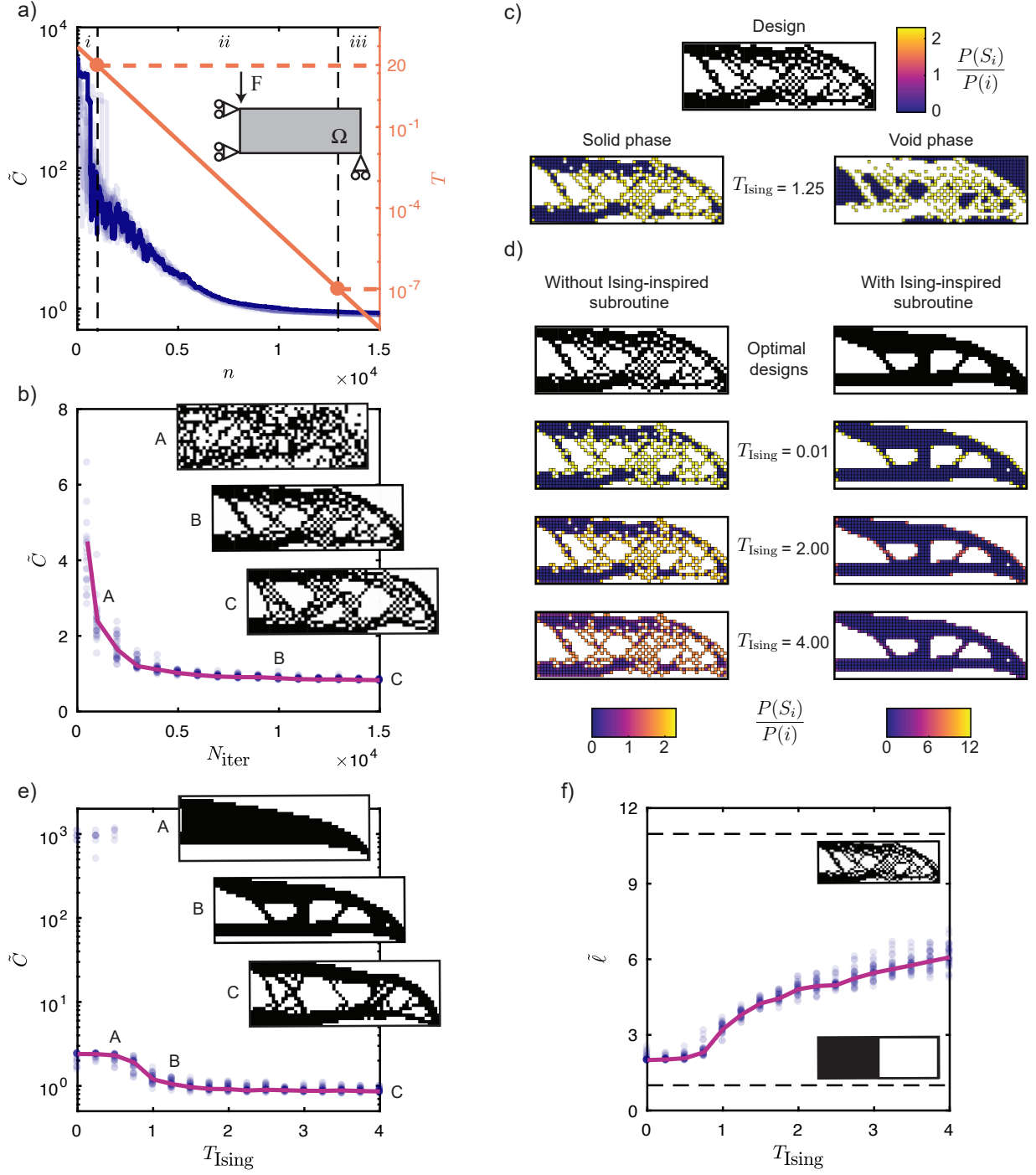


Figure 2: Compliance optimization of the MBB-beam problem using our stochastic optimization algorithm without and with Ising-inspired subroutine. a) Selecting the optimal temperature bounds (T_{\max} and T_{\min}) for the simulated annealing algorithm for actual optimization runs by performing ten different optimizations. b) Dependency of the final optimized solutions on the number of iterations N_{iter} . For each value of N_{iter} , 30 optimizations have been performed, where the insets show one of the final optimized solutions for $N_{\text{iter}} = 10^3$, 10^4 and $1.5 \cdot 10^4$. c) Probability distribution of the Ising-inspired subroutine to change the density of an element as determined from Eq. (9) within a solid or void phase, relative to the optimal solution B in Fig. 2b. d) Effect of Ising temperature on the swapping probability of element in the solid phase for optimized solutions found without and with the Ising-inspired subroutine. e) Dependency of the final optimized solutions on the Ising temperature T_{Ising} . For each value of T_{Ising} , 30 optimizations have been performed, where the insets show one of the final optimized solutions for $T_{\text{Ising}} = 0.5$, 1.25 and 4 . f) Length of the material-void interface for the optimized solutions. The insets represent the bounds for the length.

To ensure that the volume constraint is satisfied, each design change is divided in two steps in which we first draw a solid element, update the density and probability distribution, and then we draw a void element. In Figure 2c we show the material and void probability distributions of an optimized design with a checkerboard pattern, in which the density distributions are normalized with respect to the probability of a random element selection $P(i)$ (i.e. without using the Ising-inspired subroutine). Moreover, in Fig. 2d we show the effect of T_{Ising} on the probability of making a solid element void for the given configuration. We observe that for low T_{Ising} , the elements located at the solid-void interface (e.g. checkerboard regions) have a high probability of being swapped, while the elements within homogeneous regions have almost zero probability. Increasing the temperature will increase the probability of selecting elements within the homogeneous regions, which in the limit of $T_{\text{Ising}} \rightarrow \infty$ results in a fully random selection not influenced by the Ising-inspired subroutine.

We next apply this subroutine to the same compliance optimization problem considered previously, using the same parameters for the simulated annealing algorithm, and study the effect of T_{Ising} on the optimized topology. We do so by running 30 simulations per T_{Ising} value. As can be seen in Fig. 2e, for low T_{Ising} the material clusters dramatically, and prevents full exploration of the design space. As a result, the optimized designs have a relatively high compliance of $\tilde{C} \approx 2.4$. Moreover, for $T_{\text{Ising}} < 0.5$ we find that some optimized designs are disconnected from the boundary conditions (i.e. connected via low density elements), leading to very high objective values of $\tilde{C} \approx 10^3$. Better results are obtained for $T_{\text{Ising}} \geq 1$, for which all the optimizations converge to similar objective function values of $\tilde{C} \approx 0.9$, comparable to the results obtained

without Ising-inspired subroutine.

Interestingly, while the objective functions for $T_{\text{Ising}} > 1$ found with our stochastic optimization approach are similar, the optimized topologies depend greatly on T_{Ising} . Two examples for which we have used $T_{\text{Ising}} = 1.25$ and $T_{\text{Ising}} = 4$ are shown in Fig. 2e. Clearly, lower T_{Ising} results into more clustered solutions and mitigates the checkerboard patterns, while high T_{Ising} creates thin material connections with sharp material-void interfaces affected by numerical errors. This effect of T_{Ising} on the topology can be shown by considering the final length $\tilde{\ell} = \ell/\ell_{\min}$ of the solid-void interface as shown in Fig. 2f, where the lower dashed line represents the minimum length ℓ_{\min} the given domain can achieve, and the upper dashed line is the length of the optimal design obtained without the Ising-inspired subroutine shown in Fig. 2c. For $T_{\text{Ising}} > 1$ we find a direct relation between the Ising temperature and the interface length. Taking both effects into account, we select $T_{\text{Ising}} = 1.25$ as the temperature in the following studies. Note that the results obtained for $T_{\text{Ising}} = 1.25$ are $\sim 30\%$ higher, and therefore not as good as, the optimal material distribution obtained with the SIMP method [38], see Section 3 of SI.

Furthermore, besides reducing the interface length and removing checkerboard patterns, introducing the Ising-inspired subroutine heuristically reduces the number of candidate solutions that are considered during each iteration of the optimization. This is shown in Fig. 2d, where we plot the probability of selecting elements of an optimal design obtained with the Ising-inspired subroutine. Notice how the elements with high probability of being swapped are mostly at the material-void interface. Therefore, the optimization first explores the interesting part of the design space, associated with the material interface

rather than considering the full domain at each iteration.

Buckling behavior optimization

The strength of our algorithm becomes visible when dealing with disjoint problems, where conventional gradient-based approaches fail. In this section we will focus on determining the topology of a periodic structure that undergoes buckling. We focus on a beam-like domain composed of $n_x^{\text{uc}} \times n_y^{\text{uc}} = 2 \times 10$ unit cells, in which each unit cell is made of $n_x \times n_y = 20 \times 20$ elements that are used as the design variables. We fix the top and bottom of the beam, and apply a vertical compression. Moreover, to better estimate the bifurcation buckling we impose mirror symmetry with respect to the vertical axis for the density distribution [44] (see schematic in Fig. 3a).

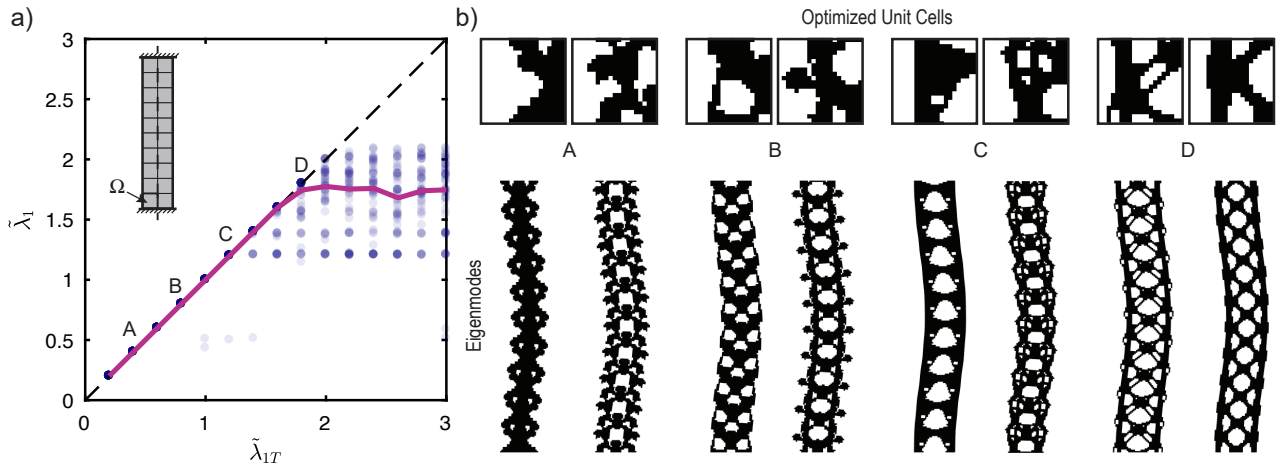


Figure 3: Optimization to a target buckling load $\tilde{\lambda}_{1T}$. a) Results of 900 optimizations (60 per selected $\tilde{\lambda}_{1T}$) as a function of the target value $\tilde{\lambda}_{1T}$. b) Selection of optimal density distributions and the corresponding buckling modes for $\tilde{\lambda}_{1T} = 0.4, 0.8, 1.2$ and 1.8 .

Optimizing for a specific buckling load

We start by determining the optimal topology of the periodic beam for a pre-defined buckling load. Given a target critical force, the optimization problem

can be defined as:

$$\min_{\rho_i} \quad \Phi(\rho_i) = \sqrt{(\lambda_1 - \lambda_{1T})^2} \quad (10a)$$

$$s.t. \quad ([\mathbf{K}] - \boldsymbol{\lambda}[\mathbf{K}_\sigma]) \{\boldsymbol{\delta D}\} = \{\mathbf{0}\}, \quad \{\boldsymbol{\delta D}\} \neq \{\mathbf{0}\} \quad (10b)$$

$$\boldsymbol{\lambda} = \{\lambda_1, \lambda_2, \dots, \lambda_n\}^T \quad (10c)$$

$$\frac{V_{\text{solid}}}{V_\Omega} = \phi^* = 0.5, \quad (10d)$$

where λ_1 is the first eigenvalue, λ_{1T} is the target eigenvalue, and $[\mathbf{K}]$ and $[\mathbf{K}_\sigma]$ are the stiffness matrix and the geometrical stiffness matrix, respectively (see Sec. 1 of the SI). The eigenvalues $\boldsymbol{\lambda}$ are coefficients proportional to the buckling force of the structure. Note that we consider only positive eigenvalues related to compression of the beam, and ignore negative eigenvalues related to tension. Furthermore, by performing the same parameter study as done in previous sections for the compliance optimization problem, we obtain suitable temperatures for this problem given by $T_{\text{max}} = 0.01$, $T_{\text{min}} = 10^{-8}$ and $N_{\text{iter}} = 3000$. Finally, we use $T_{\text{Ising}} = 1.25$ as determined previously.

In Figure 3a we show the results of 900 optimizations for $\tilde{\lambda}_{1T} = \lambda_{1T}/\lambda_{\text{ref}}$ in the range $[0.2, 3]$, where λ_{ref} is the first buckling load of a solid beam with equal volume fraction ϕ^* . We find that our algorithm can consistently optimize for targeted buckling forces up to $\tilde{\lambda}_{1T} \approx 1.3$ (i.e. the buckling force is improved by 30% with respect to a solid beam made with the same mass), where we find that approximately 1% percent of simulation converges to a load different than the objective. Interestingly, for each target buckling force we find multiple optimal solutions, as shown by the examples in Fig. 3b. However, for $\tilde{\lambda}_{1T} > 1.3$ (i.e. $\tilde{\lambda}_1 > 1.3$) we see an increase in diversity, resulting from solutions that do not converge to the target objective. In fact, these solutions are likely the result

of optimizations that converge to local minima. Note that for $\tilde{\lambda}_{1T} > 2$ we find that all solutions convergence to a value lower than the target, with a median value at $\tilde{\lambda}_1 \approx 1.8$.

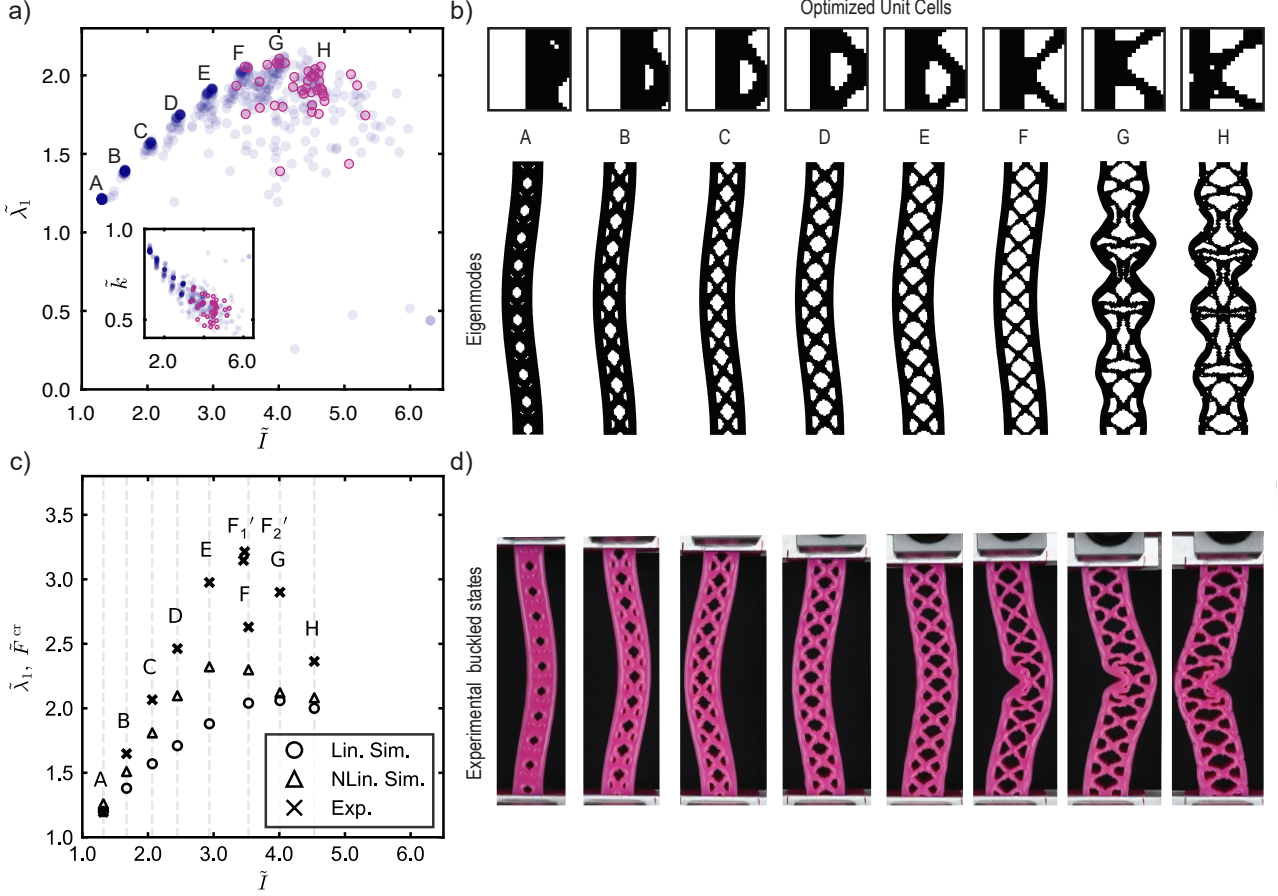


Figure 4: Maximum buckling load optimization. a) The buckling load $\tilde{\lambda}_1$ of 600 optimization in function of the optimized structures' normalized moment of inertia \tilde{I} . Structures with first modes characterized by long ($2n_y^{uc}L$) or short ($2L$) wavelengths are indicated by the blue and pink markers, respectively. The insets shows the effective stiffness \tilde{k} of the optimized solutions. b) Representative unit cells and buckling modes of structures A-H. c) and experiments (\tilde{F}^{cr}). d) Experimentally obtained buckled state of the representative geometries A-H.

Maximizing buckling load

To understand whether the maximum buckling load we achieved for this domain is $\tilde{\lambda}_1 \approx 2$ as we showed in the previous section, or that this limit is an artefact of the convergence to local minima, we next introduce an optimization problem to maximize the buckling load. This is achieved by setting the target objec-

tive buckling force in Eq. (10a) to an arbitrarily high value of $\tilde{\lambda}_{1T}=10$, which effectively will never be reached. Movie 1 and 2 of the SI show the accepted candidate solutions of two optimizations, with and without Ising-inspired subroutine, respectively. It is important to note that during both optimization paths we encounter buckling modes of different wavelengths, indicating the disjoint nature of the problem.

We perform 600 optimizations, each starting from different random initial configurations. The results are shown in Fig. 4a, in which we plot the normalized buckling force $\tilde{\lambda}_1$ and average moment of inertia $\tilde{I} = \langle I \rangle / \langle I_{\text{ref}} \rangle$ for each optimized beam, where $\langle I \rangle = \iiint \rho_i x_i^2 dA dy$. As expected, we find that most of the results are clustered within a few local minima indicated by points A-H in Fig. 4a. Representative topologies for these local minima are shown in Fig. 4b. We find that in order to achieve higher buckling force the material distribution needs to maximize the moment of inertia, which follows Timoshenko beam theory [45]. As a consequence, an increase in buckling force lowers the stiffness of the structures as shown in the inset of Fig. 4a. For beams with lower moment of inertia (e.g. beams A-F) we find that all optimized beams buckle with a wavelength equal to $2n_y^{\text{uc}}L$. However, we also observe solutions (e.g. beams G-H) in which the first buckling mode has a wavelength equal to double the size of the unit cell ($2L$), similar to the observation made in Fig. 1. This is the result of widening of the beams, which has a direct impact on the thickness and buckling behavior of the internal features. By performing centroid linkage hierarchical clustering on the eigenvector results [46], we are able to assess the wavelengths of optimized beams, and distinguish beams with wavelengths equal to $2n_y^{\text{uc}}L$ from $2L$ as indicated by using blue and pink markers in Fig. 4a. The

appearance of these two modes seems to limit the maximum buckling load that can be achieved, and we find a maximum buckling load equal to 2.04 times that of a solid beam with the same weight.

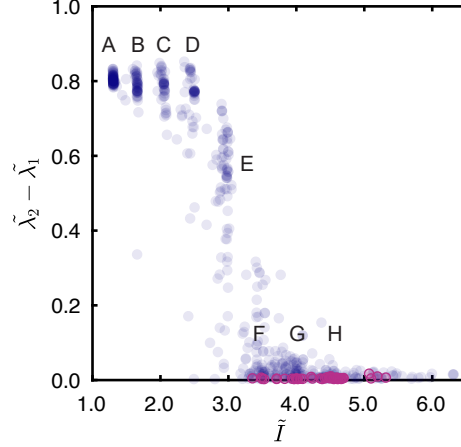


Figure 5: Difference between the buckling load of the first and second mode $\tilde{\lambda}_2 - \tilde{\lambda}_1$ of the optimized structures from Fig. 4, as a function of the moment of inertia \tilde{I} . Structures with first modes characterized by long ($2n_y^{\text{uc}}L$) or short ($2L$) wavelengths are indicated by the blue and pink markers, respectively.

Experimental validation To quantify how the optimized topologies (A-H in Fig. 4b) compare with experiments, we fabricated the beams using an elastomeric rubber (Zhermack Elite Double 8). Each beam was casted in a single step in a 3D-printed mold (Stratasys Eden260VS), and has a thickness of 40mm and a nominal length of 140mm , associated with a unit cell dimension of $14 \times 14\text{mm}$. We then performed five compression cycles at a rate of $30\text{mm}/\text{min}$ to a maximum compression of 20mm using a materials testing machine (Instron 5965L9510). From the force-displacement response we can then determine the buckling point F^{cr} , which is found at the intersection between the regression lines of the force-strain curves at small strain $\epsilon \approx 0$ and right after buckling as indicated by the sharp transition (Fig. S3a). To be able to compare the results with experiments we normalize each response by the experimental buckling force of the reference

geometry (solid vertical beam), i.e. $\tilde{F} = F/F_{\text{ref}}^{\text{cr}}$.

The results are summarized in Fig. 4c, where we show the difference between the experimental buckling force \tilde{F}_{cr} and simulation results $\tilde{\lambda}_1$ in function of the normalized moment of inertia of the structures \tilde{I} . While beam A, which is closest to a solid beam, is in agreement with the simulation results, wider beams with a more defined porous structure start to show higher buckling forces compared to the numerical results. Interestingly, for beams A-E we see an approximately linear deviation from the predicted buckling load $\tilde{\lambda}_1$ for increasing \tilde{I} . This is likely due to the relatively large strains that need to be applied before the beams buckle (i.e. up to $\epsilon = 0.12$), such that the beams considerably widen and shorten, resulting into an effective increase in the experimental buckling load. nonlinear geometrical effects have not been taken into account in the model.

, this nearly linear relation between buckling force and moment of inertia does not hold for beams F-H. To determine where this deviation is coming from, we show in Fig. 4d the experimentally obtained buckled states for all beams right after buckling has occurred. While for beams A-E the beams all buckle in the predicted buckling mode, for beams F-H we observe a localization of the mode and a sudden drop in force (Fig. S3a). This localization indicates a creasing instability [47], . Note that beams D-E also show a similar localization later along the loading path, and therefore undergo a second instability during loading. Importantly, it seems that due to the increase in buckling load of the predicted buckling mode, a mode switch occurs in beams F-H, such that for higher values of the moment of inertia the expected buckling load can no longer

be reached.

The sensitivity of the buckling mode to the finite size deformations that occur during loading suggests that the critical values of higher modes are not well separated from the first mode. In Figure 5 we show the difference between the critical force of the first and second mode $\tilde{\lambda}_2 - \tilde{\lambda}_1$, as a function of the moment of inertia \tilde{I} . Interestingly, we find a sudden transitions at $\tilde{I} = 3$ that separates structures that have a well-defined first mode (e.g. A-E), and structures for which multiple modes happen at the same critical force (e.g. F-H). Note that all the structures that exhibit potential microscopic buckling (i.e. have a buckling wavelength of $2L$ as indicated by the pink marker in Fig. 5) lay on $\tilde{\lambda}_2 - \tilde{\lambda}_1 \approx 0$, such that we were not able to obtain such a localized mode experimentally.

Penalizing higher modes

To investigate whether mode switching influences the experimental post buckling behavior of our optimized geometries, we next introduce a penalty in our optimization problem that enforces a minimum separation between the first and second critical buckling force. To do so, we rewrite the objective function from Eq. (10a) as

$$\min_{\rho_i} \quad \Phi(\rho_i) = \sqrt{\left(\tilde{\lambda}_1 - \tilde{\lambda}_{1T}\right)^2} + \alpha \frac{\delta\tilde{\lambda} - \delta\tilde{\lambda}_T}{\delta\tilde{\lambda}_T}, \quad (11)$$

in which α is the penalty factor, equal to

$$\alpha = \begin{cases} 1/5, & \text{if } \delta\tilde{\lambda} < \delta\tilde{\lambda}_T \\ 0, & \text{if } \delta\tilde{\lambda} \geq \delta\tilde{\lambda}_T. \end{cases} \quad (12)$$

For further optimization studies we chose $\delta\tilde{\lambda}_T = \tilde{\lambda}_2 - \tilde{\lambda}_1 = 0.3$ as the minimum distance between the first and second buckling mode. Rerunning the previous optimization study now with the penalty applied to the buckling force of the second mode has a considerable effect on the results. This becomes clear in Fig. 6b, in which we show the difference between the buckling force $\delta\tilde{\lambda}$ for the optimized structures in function of the moment on inertia \tilde{I} . The sharp transition at $\tilde{I} \approx 3$ is still present, however the results levels off for $\tilde{I} > 3$ at the specified minimum of $\delta\tilde{\lambda} = 0.3$. It is important to note that by using this penalty we only find structures that exhibit a macroscopic buckling mode with a wavelength of $2n_y^{\text{uc}}L$. Moreover, while we are still able to achieve structures similar to A-F found previously, Fig. 6a shows that after the introduction of the penalty, we no longer observe clusters of structures with a microstructure similar to G and H (Fig. 4a).

To assess whether the separation of the first and second mode has an effect on the buckling behavior of our structures, we fabricated two different geometries belonging to the F' group, and used to same protocol as before to test them in a compression machine. In Figure 6c we show the buckling modes of the optimized geometries F₁' and F₂' obtained using both simulations and experiments. While the designs are nearly identical to structure F (Fig. 4), these structures undergo macroscopic buckling as predicted by our simulations, before exhibiting a creasing instability, see Fig. S3b. In fact, by adding the experimental results in terms of buckling force \tilde{F}^{cr} to Fig. 4c, we find that the structures exhibit the same geometrical stiffening as predicted. Therefore, we conclude that the second mode for structures F₁' and F₂' is separated well enough to prevent mode switching.

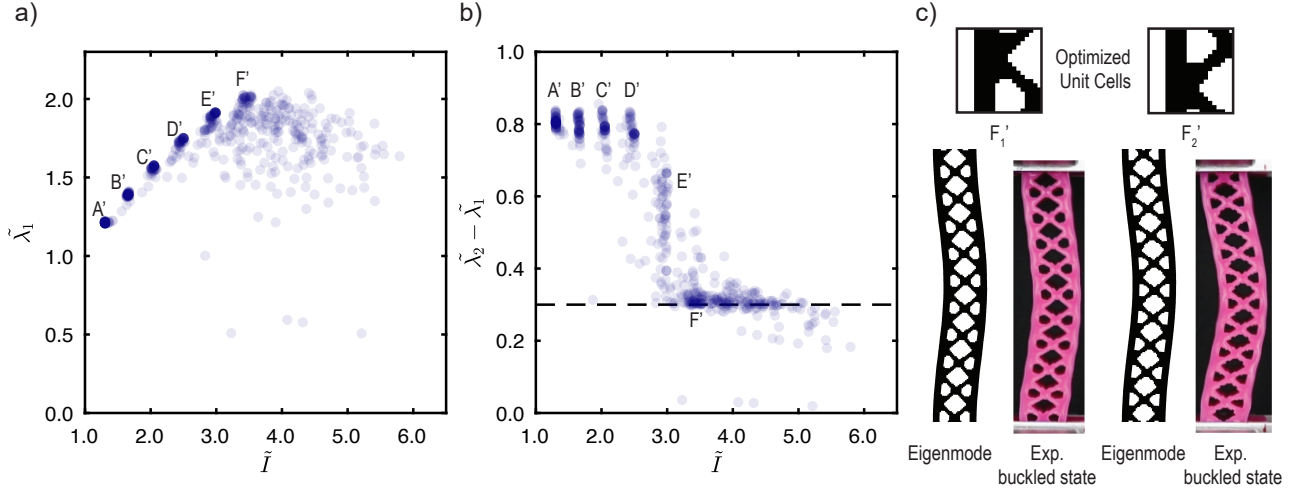


Figure 6: Maximum buckling load optimization with penalization of the second buckling mode according to Eq. 11 with $\delta\tilde{\lambda}_T = 0.3$. a) Buckling load $\tilde{\lambda}_1$ of 600 optimizations in function of average moment of inertia \tilde{I} . Most of the results cluster in the same minima A'-F' as previous maximization study without penalization, however, structures G and H are no longer present (Fig. 4a). b) Difference between the buckling load of the first and second mode $\tilde{\lambda}_2 - \tilde{\lambda}_1$ as a function of the average moment of inertia \tilde{I} . c) Comparison between buckling modes obtained using simulations and experiments for two representative geometries belonging to cluster F'.

Maximum mode separation

Finally, to explore the maximum mode separation that can be achieved between the first two modes, we introduce a different objective function given by:

$$\min_{\rho_i} \quad \Phi(\rho_i) = \sqrt{\left(\tilde{\lambda}_1 - \tilde{\lambda}_{1T}\right)^2 + \left(\tilde{\lambda}_2 - \tilde{\lambda}_{2T}\right)^2}. \quad (13)$$

We ran a total of 2104 optimizations with target eigenvalues ranging between $\tilde{\lambda}_{1T} = [0.4, 2.4]$ and $\tilde{\lambda}_{2T} = [\tilde{\lambda}_{1T}, 3]$. In Figure 7 we show the results in term of the optimized buckling forces $\tilde{\lambda}_1$ and $\tilde{\lambda}_2$. Interestingly, we find a bounded region of buckling behavior that can be achieved, indicated by the gray area. In fact, while we can optimize for structures with coincident critical points $\tilde{\lambda}_1 \approx \tilde{\lambda}_2$ resulting in so-called frustrated structures [48], there is a maximum separation $\tilde{\lambda}_2 - \tilde{\lambda}_1$ which can be achieved. This value seems to be dependent on the $\tilde{\lambda}_1$, since for $\tilde{\lambda}_1 < 1$ the maximum separation achievable $\tilde{\lambda}_2 - \tilde{\lambda}_1 \propto \tilde{\lambda}_1$, and for

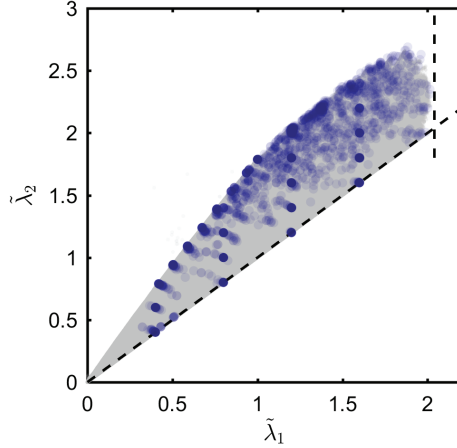


Figure 7: Optimization results for 56 different combinations of target buckling values $(\tilde{\lambda}_{1T}, \tilde{\lambda}_{2T})$, where $\tilde{\lambda}_{1T} = [0.4, 2.4]$ and $\tilde{\lambda}_{2T} = [\tilde{\lambda}_{1T}, 3]$. The blue markers indicate all optimized solutions, while the gray area shows all the evaluated solutions during the optimization, indicating the feasible design space for our optimization problem. The diagonal dashed lines represent the determined bounds, specified by $\tilde{\lambda}_1 = \tilde{\lambda}_2$, and $\tilde{\lambda}_1 < 2.1$.

$\tilde{\lambda}_1 > 1$, $\tilde{\lambda}_2 - \tilde{\lambda}_1 \propto \tilde{\lambda}_1 + 0.85$. These results are coherent with the results shown in Fig. 5 and Fig. 6b. Therefore, the gray area shown in Fig. 7 represents a projection of the design space onto the control variables of our inverse design problem.

Conclusions

In this work we have . Furthermore, in order to create feasible optimized geometries, we proposed an Ising-inspired subroutine to effectively guide the optimization and cluster material. After testing our method and reproducing the results of a widely-used, differentiable, compliance optimization problem, we approached novel optimization problems dealing with the buckling behavior of mechanical metamaterials. Specifically, in this paper we focused on the optimization of the first two , and their interaction. As such, our method opens up new avenues for the exploration of more fundamental questions regarding frustration and mode interaction that occur in these and more complex mechanical

metamaterials.

Moreover, does not require objective function differentiability, it can be applied to different problems that would be impossible otherwise. These can range from of mechanical metamaterials . Therefore, we believe that the flexibility and simplicity of our method is a good addition to existing gradient-based optimization problems, and is able to deal with more complex problems that have been left unexplored so far.

Acknowledgements: This work is part of the Dutch Research Council (NWO) and was performed at the research institute AMOLF. It is part of the research program Innovational Research Incentives Scheme Veni from NWO with project number 15868 (NWO).

References

- [1] D. R. Smith, J. B. Pendry, and M. C. K. Wiltshire. Metamaterials and Negative Refractive Index. *Science*, 305(August):788–792, 2004.
- [2] J. B. Pendry. Negative refraction makes a perfect lens. *Physical Review Letters*, 85(18):3966–3969, 2000.
- [3] R. Lakes. Foam Structures with a Negative Poisson’s Ratio. *Science*, 235(4792):1038–1040, 1987.
- [4] Xiaoyu Zheng, H Lee, T H Weisgraber, M Shusteff, J DeOtte, E B Duoss, J D Kuntz, M M Biener, Q Ge, J A Jackson, S O Kucheyev, N X Fang, and

- C M Spadaccini. Ultralight, Ultrastiff Mechanical Metamaterials. *Science*, 344(6190):1373–1377, 2014.
- [5] Tolga Ergin, Nicolas Stenger, Patrice Brenner, John B Pendry, and Martin Wegener. Three-dimensional invisibility cloak at optical wavelengths. *Science (New York, N.Y.)*, 328(5976):337–9, 2010.
- [6] Tiemo Bückmann, Muamer Kadic, Robert Schittny, and Martin Wegener. Mechanical cloak design by direct lattice transformation. *Proceedings of the National Academy of Sciences*, 112(16):4930–4934, 2015.
- [7] Bastiaan Florijn, Corentin Coullais, and Martin Van Hecke. Programmable mechanical metamaterials. *Physical Review Letters*, 113(17), 2014.
- [8] Katia Bertoldi, Reis Pedro M., Willshaw Stephen, and Mullin Tom. Negative poisson’s ratio behavior induced by an elastic instability. *Advanced Materials*, 22(3):361–366, 2010.
- [9] K. Bertoldi and M. C. Boyce. Mechanically triggered transformations of phononic band gaps in periodic elastomeric structures. *Phys. Rev. B*, 77:052105, Feb 2008.
- [10] Johannes TB Overvelde and Katia Bertoldi. Relating pore shape to the non-linear response of periodic elastomeric structures. *Journal of the Mechanics and Physics of Solids*, 64:351–366, 2014.
- [11] Jongmin Shim, Sicong Shan, Andrej Kosmrlj, Sung H. Kang, Elizabeth R. Chen, James C. Weaver, and Katia Bertoldi. Harnessing instabilities for design of soft reconfigurable auxetic/chiral materials. *Soft Matter*, 9:8198–8202, 2013.

- [12] Shan Sicong, Kang Sung H., Wang Pai, Qu Cangyu, Shian Samuel, Chen Elizabeth R., and Bertoldi Katia. Harnessing multiple folding mechanisms in soft periodic structures for tunable control of elastic waves. *Advanced Functional Materials*, 24(31):4935–4942, 2014.
- [13] Martin Philip Bendsøe and Noboru Kikuchi. Generating optimal topologies in structural design using a homogenization method. *Computer Methods in Applied Mechanics and Engineering*, 71(2):197 – 224, 1988.
- [14] Ole Sigmund and Kurt Maute. Topology optimization approaches. *Structural and Multidisciplinary Optimization*, 48(6):1031–1055, Dec 2013.
- [15] V.J. Challis, A.P. Roberts, and A.H. Wilkins. Design of three dimensional isotropic microstructures for maximized stiffness and conductivity. *International Journal of Solids and Structures*, 45(14):4130 – 4146, 2008.
- [16] M. M. Neves, H. Rodrigues, and J. M. Guedes. Generalized topology design of structures with a buckling load criterion. *Structural optimization*, 10(2):71–78, Oct 1995.
- [17] David C. Dobson and Steven J. Cox. Maximizing band gaps in two-dimensional photonic crystals. *SIAM Journal on Applied Mathematics*, 59(6):2108–2120, 1999.
- [18] Ole Sigmund and Jakob Søndergaard Jensen. Systematic design of phononic band-gap materials and structures by topology optimization. *Philosophical Transactions of the Royal Society of London. Series A: Mathematical, Physical and Engineering Sciences*, 361(1806):1001–1019, 2003.

- [19] Jakob S. Jensen and Ole Sigmund. Systematic design of photonic crystal structures using topology optimization: Low-loss waveguide bends. *Applied Physics Letters*, 84(12):2022–2024, 2004.
- [20] Ole Sigmund and Kristian Hougaard. Geometric properties of optimal photonic crystals. *Phys. Rev. Lett.*, 100:153904, Apr 2008.
- [21] Søren Halkjær, Ole Sigmund, and Jakob S Jensen. Inverse design of phononic crystals by topology optimization. *Zeitschrift für Kristallographie-Crystalline Materials*, 220(9-10):895–905, 2005.
- [22] O. Sigmund and S. Torquato. Composites with extremal thermal expansion coefficients. *Applied Physics Letters*, 69(21):3203–3205, 1996.
- [23] Anders Clausen, Fengwen Wang, Jakob S Jensen, Ole Sigmund, and Jennifer A Lewis. Topology optimized architectures with programmable poisson’s ratio over large deformations. *Advanced Materials*, 27(37):5523–5527, 2015.
- [24] Hao Deng, Lin Cheng, Xuan Liang, Devlin Hayduke, and Albert C To. Topology optimization for energy dissipation design of lattice structures through snap-through behavior. *Computer Methods in Applied Mechanics and Engineering*, 358:112641, 2020.
- [25] Thomas Borrvall and Joakim Petersson. Topology optimization of fluids in stokes flow. *International journal for numerical methods in fluids*, 41(1):77–107, 2003.
- [26] Xingjun Gao and Haitao Ma. Topology optimization of continuum structures under buckling constraints. *Computers & Structures*, 157:142–152, 2015.

- [27] Christian Rye Thomsen, Fengwen Wang, and Ole Sigmund. Buckling strength topology optimization of 2d periodic materials based on linearized bifurcation analysis. *Computer Methods in Applied Mechanics and Engineering*, 339:115–136, 2018.
- [28] Ole Sigmund. On the usefulness of non-gradient approaches in topology optimization. *Structural and Multidisciplinary Optimization*, 43(5):589–596, 2011.
- [29] David Victor Hinkley and DR Cox. *Theoretical statistics*. Chapman and Hall/CRC, 1979.
- [30] D Pihler-Puzović, AL Hazel, and Tom Mullin. Buckling of a holey column. *Soft matter*, 12(34):7112–7118, 2016.
- [31] Chris G Johnson, Utkarsh Jain, Andrew L Hazel, D Pihler-Puzović, and Tom Mullin. On the buckling of an elastic holey column. *Proc. R. Soc. A*, 473(2207):20170477, 2017.
- [32] Martin P Bendsøe. Optimal shape design as a material distribution problem. *Structural optimization*, 1(4):193–202, 1989.
- [33] Martin P. BendsøeOle Sigmund. *Topology Optimization Theory, Methods, and Applications*. Springer, 2004.
- [34] Patrick Y Shim and Souran Manoochehri. Generating optimal configurations in structural design using simulated annealing. *International journal for numerical methods in engineering*, 40(6):1053–1069, 1997.
- [35] Scott Kirkpatrick, C Daniel Gelatt, and Mario P Vecchi. Optimization by simulated annealing. *Science*, 220(4598):671–680, 1983.

- [36] Yaghout Nourani and Bjarne Andresen. A comparison of simulated annealing cooling strategies. *Journal of Physics A: Mathematical and General*, 31(41):8373, 1998.
- [37] Niels Olhoff, Martin P Bendsøe, and John Rasmussen. On cad-integrated structural topology and design optimization. *Computer Methods in Applied Mechanics and Engineering*, 89(1-3):259–279, 1991.
- [38] Ole Sigmund. A 99 line topology optimization code written in matlab. *Structural and multidisciplinary optimization*, 21(2):120–127, 2001.
- [39] Ole Sigmund and Joakim Petersson. Numerical instabilities in topology optimization: a survey on procedures dealing with checkerboards, mesh-dependencies and local minima. *Structural optimization*, 16(1):68–75, 1998.
- [40] Alejandro Diaz and Ole Sigmund. Checkerboard patterns in layout optimization. *Structural optimization*, 10(1):40–45, 1995.
- [41] Ole Sigmund. *Design of material structures using topology optimization*. PhD thesis, Technical University of Denmark Denmark, 1994.
- [42] Ernst Ising. Beitrag zur theorie des ferromagnetismus. *Zeitschrift für Physik*, 31(1):253–258, 1925.
- [43] Stephen G Brush. History of the lenz-ising model. *Reviews of modern physics*, 39(4):883, 1967.
- [44] Bernard Budiansky. Theory of buckling and post-buckling behavior of elastic structures. *Advances in applied mechanics.*, 14:1–65, 1974.
- [45] Stephen P Timoshenko and James M Gere. *Theory of elastic stability*. Courier Corporation, 2009.

- [46] Stephen C Johnson. Hierarchical clustering schemes. *Psychometrika*, 32(3):241–254, 1967.
- [47] Evan Hohlfeld and Lakshminarayanan Mahadevan. Unfolding the sulcus. *Physical review letters*, 106(10):105702, 2011.
- [48] Sung Hoon Kang, Sicong Shan, Andrej Košmrlj, Wim L Noorduin, Samuel Shian, James C Weaver, David R Clarke, and Katia Bertoldi. Complex ordered patterns in mechanical instability induced geometrically frustrated triangular cellular structures. *Physical review letters*, 112(9):098701, 2014.